crystals

MDPI

Article

Effect of Picosecond Laser Diverse Scanning Strategies in Fabrication of Broadband AntiReflection Structures on Copper

Jie Zhao, Zehao Cao, Yilongrui Chen and Zongtai He *

Laser Group, School of Mechanical Engineering, Hubei University of Technology, Wuhan 430068, China; 102310036@hbut.edu.cn (J.Z.); 502400006@hbut.edu.cn (Z.C.); 102510098@hbut.edu.cn (Y.C.)
* Correspondence: 201910115@hbut.edu.cn

Abstract

Broadband antireflective surface technology constitutes a crucial technique in optoelectronic devices, playing a key role in reducing optical losses. Ultrafast laser processing provides a flexible route for fabricating micro-nano structures on metallic surfaces because it enables efficient fabrication, high spatial resolution, and minimal chemical consumption. This study uses a variable-angle scanning strategy to texture the copper surface, produce a series of antireflection arrayed micro-nano structures, and study the spectral reflectance characteristics of the copper surface. The results exhibit that 90° orthogonal scanning favors the formation of an arrayed microcone structure, which shows lower reflectance than the non-orthogonal scanning strategies in the 200–1300 nm band, with a minimum reflectance of 0.94%. The 60° and 45° cross-scanning based on the non-orthogonal strategy favors the formation of microcavity structures, and shows low reflectance in the 1300–2500 nm band, with the maximum reflectance remaining below 5%. Laser-induced periodic surface structures (LIPSS) are observed on the structures fabricated by all strategies. This work demonstrates that the scanning angle itself can be used to switch the dominant surface morphology and thereby tailor the spectral antireflection response, and lies in establishing a clear processing–structure–spectral response relationship for copper surfaces, which provides a designable route for wavelength-selective optical absorption in photothermal conversion, infrared detection, and sensing applications.

Keywords: copper; ultrafast laser; diverse scanning strategy; broadband antireflection; micro-nano hierarchical structures

1. Introduction

Copper is an important functional material widely used in applications including solar selective absorbers, infrared sensing, aerospace, and radiative heat transfer. Achieving broadband antireflection on copper surfaces is crucial to improve the photothermal effect of the device [1,2]. Traditional antireflective surface preparation methods include surface roughening and coating-based approaches [3]. These approaches are often limited by the difficulty of accurately controlling surface morphology, insufficient durability, and potential environmental burden. In recent years, laser surface texturing has offered micron-level precision and excellent controllability for the fabrication of surface micro-nanostructures, and it has attracted widespread attention [4–10].

Previous studies have shown that by controlling parameters including laser wavelength and pulse duration, multi-scale structures from nanoscale to micron scale can be

Check for updates

Academic Editor: José L. García

Received: 4 April 2026
Revised: 24 April 2026
Accepted: 28 April 2026
Published: 30 April 2026

Copyright: © 2026 by the authors. Licensee MDPI, Basel, Switzerland. This article is an open access article distributed under the terms and conditions of the Creative Commons Attribution (CC BY) license.

prepared on the metal surface, thereby significantly reducing the reflectivity in the broadband spectral range [4,11,12]. He et al. used a nanosecond laser to fabricate micro-nano structures on the copper surface, achieving an average reflectance of 1.1% in the 220–800 nm band and an average reflectance of 8.1% in the 220–2500 nm band [11]. Qi et al. used a femtosecond laser for layered "V" scanning, and achieved a uniformly low reflectance of less than 2% in the 200 nm to 25 my band [12]. In the process of laser preparation of micro-nanostructures on metal surfaces, micron-scale cones, holes, or microcavities are effective geometric light-trapping units [5], and subwavelength nanostructures, such as nanoparticles, can further suppress light reflection through the effective medium effect or surface plasmon resonance [13,14]. Therefore, multi-scale structuring assisted by a specific environment is considered a key strategy to achieve ultra-wideband and low reflection [5,15]. Long et al. proposed that resolidified materials and plasma redeposition during laser processing are responsible for the formation of large-scale micropillars and nanoparticle agglomerates [16]. The synergistic effect between ultrafast laser, liquid environment, and in-situ chemical oxidation is considered to be an effective method to construct ultra-precise hierarchical structures such as sea urchins [4,6,17,18].

In order to further elucidate the structure-optical response relationship, it is necessary to further study the quantitative correlation between structural morphology (including array period, depth, and hole regularity) and metal surface antireflection performance [19–22]. In previous methods, laser processing can be used to prepare holes and microcavities, but these methods remain limited by process complexity and insufficient structural diversity [16,23,24]. Fan et al. designed a cross-scan overlapping strategy on the copper surface, superimposing nanoparticles on the micron-scale substrate structure to form a disordered coral-like morphology [6]. Nayak et al. used the laser-induced self-assembly mechanism to prepare conical "forest" structures on the silicon surface [25]. Qiao et al. prepared grouped periodic structures on tungsten [26]. Ng et al. used point-by-point scanning technology to prepare blackbody cavity structures on metals [27]. Nevertheless, these approaches are still constrained by the problems of complex processes, low preparation efficiency, and difficulty in widespread application.

In this work, we show that simply changing the scanning angle can drive a controllable transition in the dominant surface architecture and thereby produce distinct wavelength-dependent antireflection characteristics on copper. The scanning strategy itself can serve as a direct morphology-control parameter: 90° orthogonal scanning promotes microcone arrays, whereas 60° and 45° non-orthogonal scanning favor microcavity-dominated structures. More importantly, these morphology differences are associated with different spectral advantages, enabling short-wavelength-dominant (UV-VIS) and long-wavelength-dominant (NIR) antireflection behaviors on the same copper substrate. This study therefore establishes a processing–structure–optical response relationship for spectral-selective reflectance tuning, providing a more designable route for copper-based functional optical surfaces.

2. Materials and Methods

2.1. Materials and Devices

T1 copper was used as the substrate in this study, with a Cu content of $\geq$99.95 wt.% and a total impurity content of $\leq$0.05 wt.%. The chemical composition is listed in Table 1. With its high purity and excellent electrical and thermal conductivity, it is widely used in electrical and thermal engineering applications. In this study, the copper substrates (Guangfeng Metal Materials Co., Ltd., Dongguan, China) were cut into 50 × 50 × 1 mm^3 specimens, and both sides were polished. Before laser processing, the samples were ultrasonically cleaned in ethanol for 15 min to remove grease and residual contaminants.

Table 1. Chemical Composition of T1 Copper Sample (wt.%).

Cu	Sn	Zn	Ni	O	As	Fe	S	Pb	Sb
99.952	0.002	0.005	0.002	0.02	0.002	0.005	0.005	0.003	0.002

A picosecond infrared laser (Ws-1064-30, Langyan Optoelectronics, Hainan, China) was employed in this study, with a wavelength of λ = 1064 nm, an adjustable pulse duration τ of 1 to 10 ps, a repetition rate of 1 MHz, a maximum average power of 30 W, and a Gaussian energy distribution. After processing, the surface three-dimensional morphology and roughness of the processed samples were measured using a laser scanning confocal microscope (LSM 900, ZEISS, Jena, Germany), the micro-nano structure was observed using a scanning electron microscope (SEM, Regulus 8230, Hitachi, Tokyo, Japan), and the spectral reflectance of the untreated and laser-textured copper surfaces was measured using a spectrophotometer with an integrating sphere (UH4150, Hitachi, Tokyo, Japan) over the wavelength range of 200–2500 nm (UV-VIS-NIR), with $BaSO_4$ as the reference standard. The measured laser-textured area was 10×10 mm^2, and all reflectance measurements were carried out at the same fixed angle of incidence.

2.2. Experimental Methods

The experimental optical setup is shown in Figure 1a. The laser beam, linearly polarized in the horizontal direction, was expanded to a diameter of 5 mm by a beam expander, redirected by a mirror to an x–y galvanometer scanner, and focused onto the upper surface of the sample through a field lens (f = 100 mm). The focused spot diameter was approximately 30 μm, defined at the $1/e^2$ intensity level of the maximum intensity. As shown in Figure 1b, three scanning strategies were adopted, including 90° orthogonal scanning, 60° cross-scanning, and 45° cross-scanning. Since the relative angle of the x–y galvo mirrors was not 45°, the laser linear polarization direction on the sample was tilted by 20° relative to the *X*-axis of the sample (indicated by the blue arrow in Figure 1b). The detailed laser-processing parameters employed for different scanning strategies are summarized in Table 2. The experiment was conducted at room temperature and atmospheric pressure. After processing, the samples were ultrasonically cleaned with ethanol and dried with compressed air to remove residual debris and loose oxides for subsequent morphology characterization and optical testing.

Table 2. Fixed laser-processing parameters and processing parameters under different scanning strategies.

Parameter Category	Parameter Value	Unit	Parameter Category	Parameter Value	Unit
Repetition rate	1	MHz	Pulse width	10	ps
Spot size	30	μm	Line interval	35	μm
Parameter category			90° scanning	60° scanning	45° scanning
Pulse energy			9–29 μJ	9–15 μJ	9–15 μJ
Scan speed			90 mm/s	5–100 mm/s	5–85 mm/s
Number of scans			10	1	1

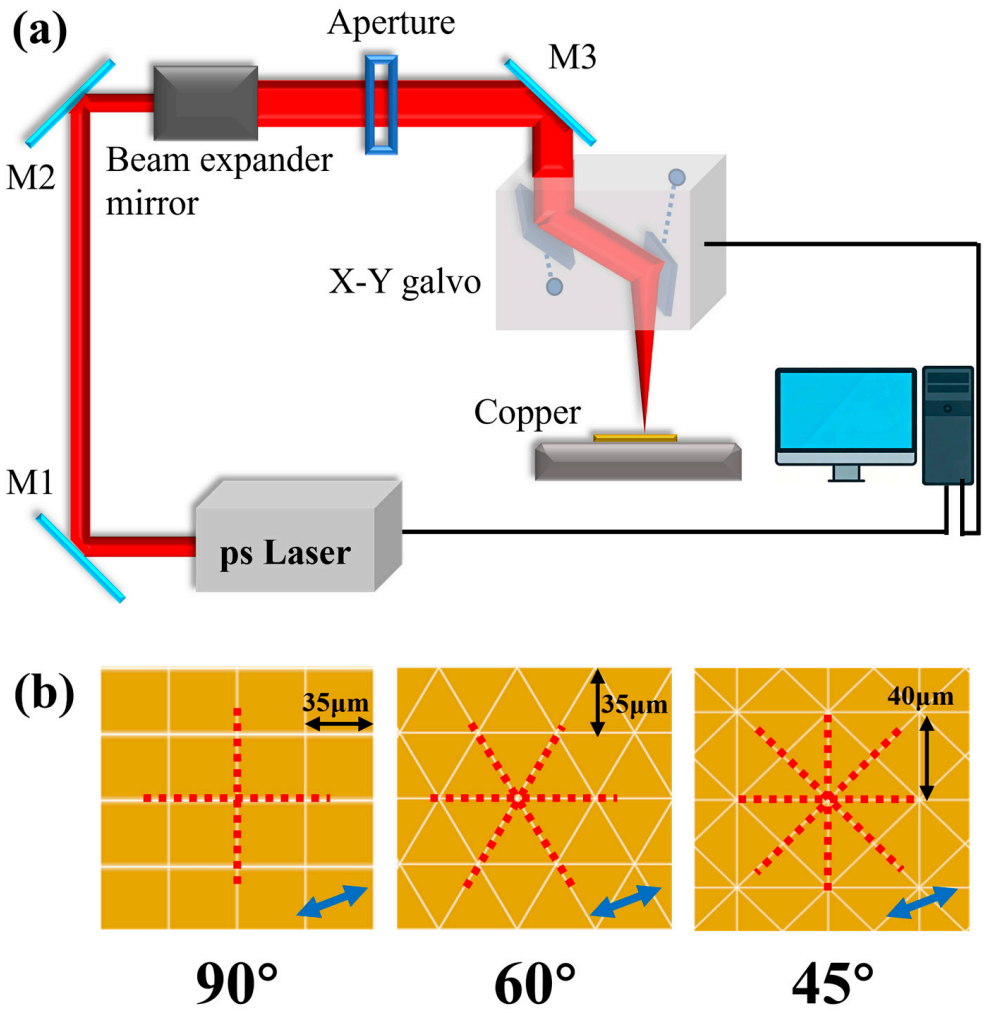


Figure 1. (**a**) Schematic diagram of the picosecond laser processing system, (**b**) Scan path schematic: 90° scanning strategy, 60° scanning strategy, and 45° scanning strategy. The two-way arrow (blue) represents the direction of laser linear polarization.

3. Results and Discussion

3.1. Orthogonal Scanning Strategy

A microcone array structure was fabricated under the 90° orthogonal scanning strategy, and the representative cross-sectional profile of a single unit is shown in Figure 2a. During repeated irradiation, regions with energy peaks preferentially undergo melting and ablation, forming periodic grooves, while areas with energy valleys are preserved, giving rise to the microcone structures. A pulse overlap ratio of 99.7% was adopted, meaning that adjacent pulses interacted extensively with the region affected by preceding pulses. Under such an extremely high overlap condition, the same region experiences repeated irradiation, and the surface evolution was governed primarily by cumulative multi-pulse interactions rather than isolated single-pulse ablation, thereby promoting melting, vaporization, and melt-assisted material removal. Meanwhile, the laser processing was performed at a repetition rate of 1 MHz, corresponding to a pulse interval of only 1 μs. As a result, successive pulses were delivered before the irradiated region could fully relax thermally, leading to pronounced heat accumulation. Under these conditions, the morphology evolution was jointly determined by ablation, melting, and redeposition, thereby facilitating the rapid formation of arrayed structures.

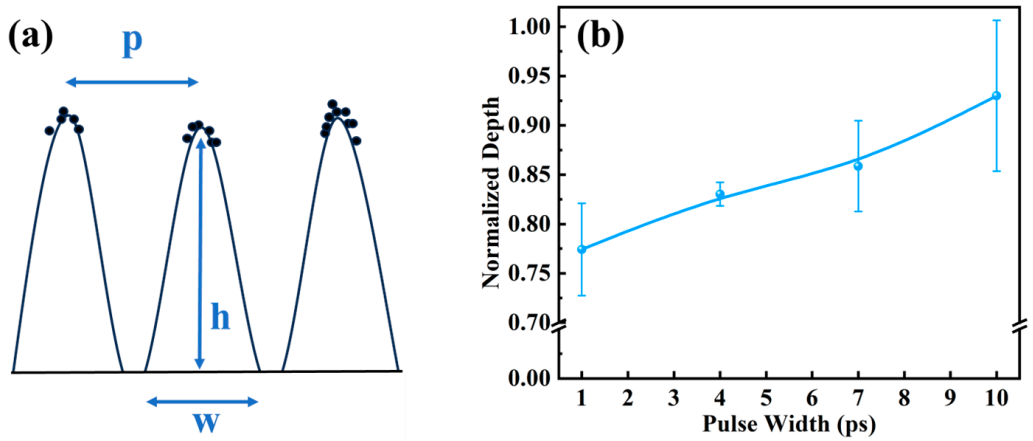


Figure 2. (**a**) Schematic diagram of the cross-sectional profile of a cone array structure, in which the cone height (h), base width (w), and period (p) are marked. Micro- and nanoparticles are distributed on the cone surface. (**b**) Normalized structural depth under different pulse duration conditions.

The reflectance of the sample is affected by the shape, period, and depth of the array structure, which are related to the laser processing parameters [13]. To clarify the effect of pulse duration on the microstructure, antireflective structures were fabricated under fixed processing conditions of a scan line interval I = 35 μm, a pulse energy E = 19 μJ (corresponding to a fluence F = 2.688 J/cm^2), a reciprocating S-shaped scanning path, and the scanning number was set to 10, while the pulse duration τ was varied from 1 ps to 10 ps. Their cross-sectional morphologies were then characterized. In order to evaluate the relationship between structural depth and pulse duration, the normalized structural depth is calculated according to Equation (1) based on the maximum depth value:

$$D = \frac{D_i}{D_m} \quad (1)$$

where D_i represents the depth of the structure at a specific pulse duration, and D_m represents the maximum depth measured under all pulse duration conditions. For each experimental condition, the structural depth was measured at five different locations on the same sample, and the mean value and standard deviation were calculated. As shown in Figure 2b, the normalized structural depth increases with the pulse duration and reaches its maximum at 10 ps, indicating a more favorable cumulative laser-material interaction under this processing condition within the investigated parameter window. This trend is consistent with the thermal penetration depth L_{th}, defined by Equation (2) [16]:

$$L_{th} = 2\sqrt{\alpha \cdot \tau} \quad (2)$$

where α is the thermal diffusivity of the material, and τ is the laser pulse duration. An increase in pulse duration leads to a larger thermal diffusion length, which means that heat has more time to propagate inside the material and facilitates material removal and melt redistribution, thereby increasing the structural depth [24]. Meanwhile, no obvious morphological deterioration was observed at 10 ps in the present experiments, suggesting that this pulse duration provides a favorable balance between sufficient structure deepening and morphology preservation. Therefore, a pulse duration of 10 ps can be regarded as an optimal condition for obtaining optically effective antireflective structures and was used in all subsequent experiments.

In order to study the effect of scan line interval on surface microstructure, the interval was set to 25 μm, 30 μm, 35 μm, and 40 μm, respectively, and the resulting surface morphologies were characterized by confocal microscopy. Five non-overlapping regions of

interest (ROI, 100 μm × 100 μm) were selected along the diagonal of the sample, and the areal root-mean-square height, Sq, of each ROI was calculated to obtain the five Sq values for each sample. The coefficient of variation, CV_{Sq}, is then calculated using Equation (3):

$$CV_{Sq} = \frac{S_{Sq}}{\mu_{Sq}} \times 100\% \quad (3)$$

where μ_{Sq} and S_{Sq} are the mean and sample standard deviation of the five Sq values, respectively. CV_{Sq} quantifies the degree of spatial dispersion of Sq within a given sample. A larger CV_{Sq} indicates poorer morphological consistency.

As shown in Figure 3a–d, at smaller scan line intervals, the overall morphological uniformity is poor. As the interval increases, the morphological uniformity improves significantly. The CV_{Sq} values in Figure 3e reflect the same trend. When the scanning interval is 25 μm, since the scanning interval is smaller than the spot diameter, multiple overlapping irradiations occurred within the same region over a short time interval, resulting in local melting and resolidified material accumulation, thereby deteriorating the structural consistency [28]. When the line interval is 30 μm, the morphology uniformity is improved. At this point, the scanning interval is consistent with the spot diameter. This interval is commonly adopted in previous studies [5,7,15,17]. However, the overlap of adjacent scanning trajectories still exists. When the scanning interval is set to be slightly larger than the spot diameter, the overall morphological uniformity is further improved, as shown in Figure 3c,d. Meanwhile, for each experimental condition, the structural depth was measured at five different locations on the same sample, and the mean value and standard deviation were calculated, as shown in Figure 3f. Under different scan line intervals, the depth of the microstructure increases with the interval, and eventually approaches saturation. However, when the scan line interval became excessively large, as shown in Figure 3d, the conical units became less sharp, and the pristine surface was retained at the top of the structures, giving the sample a grayish-white appearance at the macroscopic scale and indicating weakened antireflection performance. In general, a greater structural depth and a higher depth-to-width ratio imply stronger multiple scattering and geometrical light-trapping within the surface microstructures, which is beneficial for improving the antireflection performance of the surface [12]. However, as shown in Figure 3f, the difference in the depth-to-width ratio between the structures formed at scan line intervals of 35 and 40 μm was less than 0.05, indicating that further increasing the spacing contributed little to any additional increase in this parameter. Under these conditions, the difference in optical performance was governed more by the increase in structural period. On the one hand, this led to greater retention of the highly reflective pristine surface. On the other hand, it also increased the likelihood of incident light escaping through the gaps between adjacent structures. By contrast, a scan line interval of 35 μm provided a relatively large structural depth and a high depth-to-width ratio while minimizing the residual pristine surface. It was therefore selected as the scan line interval for the subsequent experiments.

To investigate the effect of pulse energy on surface morphology, the pulse energy was set from 9 to 29 μJ (F = 1.273–4.103 J/cm^2), and other parameters were kept unchanged. The prepared microcone array is shown in Figure 4. At low pulse energies, as shown in Figure 4a,b, the degree of material removal is limited, and the pristine surface remains at the upper end of the cell structure, which results in poor geometrical light-trapping [8]. At higher pulse energies, the absorption and scattering shielding effects associated with the laser-ablation plume, including the ejected species and debris, can attenuate subsequent incident laser pulses, leading to insufficient local energy deposition and consequently causing discontinuities and distortions of the microcone structures [7,23,29], as shown in Figure 4d,e, thereby weakening the antireflection performance. These results indicate

that increasing the pulse energy can enhance the ablation intensity and thus facilitate the formation of surface micro-nanostructures. However, an appropriate intermediate pulse energy should be selected to balance sufficient material removal with excessive plume shielding and morphology deterioration. At E = 19 μJ, a dynamic balance between ablation and redeposition is likely achieved, resulting in a relatively uniform surface morphology, as shown in Figure 4c. Under this condition, the discontinuous and distorted features that are commonly induced at higher pulse energies have not yet become dominant. Therefore, this processing parameter enables the formation of a relatively stable morphology and leads to low overall reflectance at the macroscopic scale.

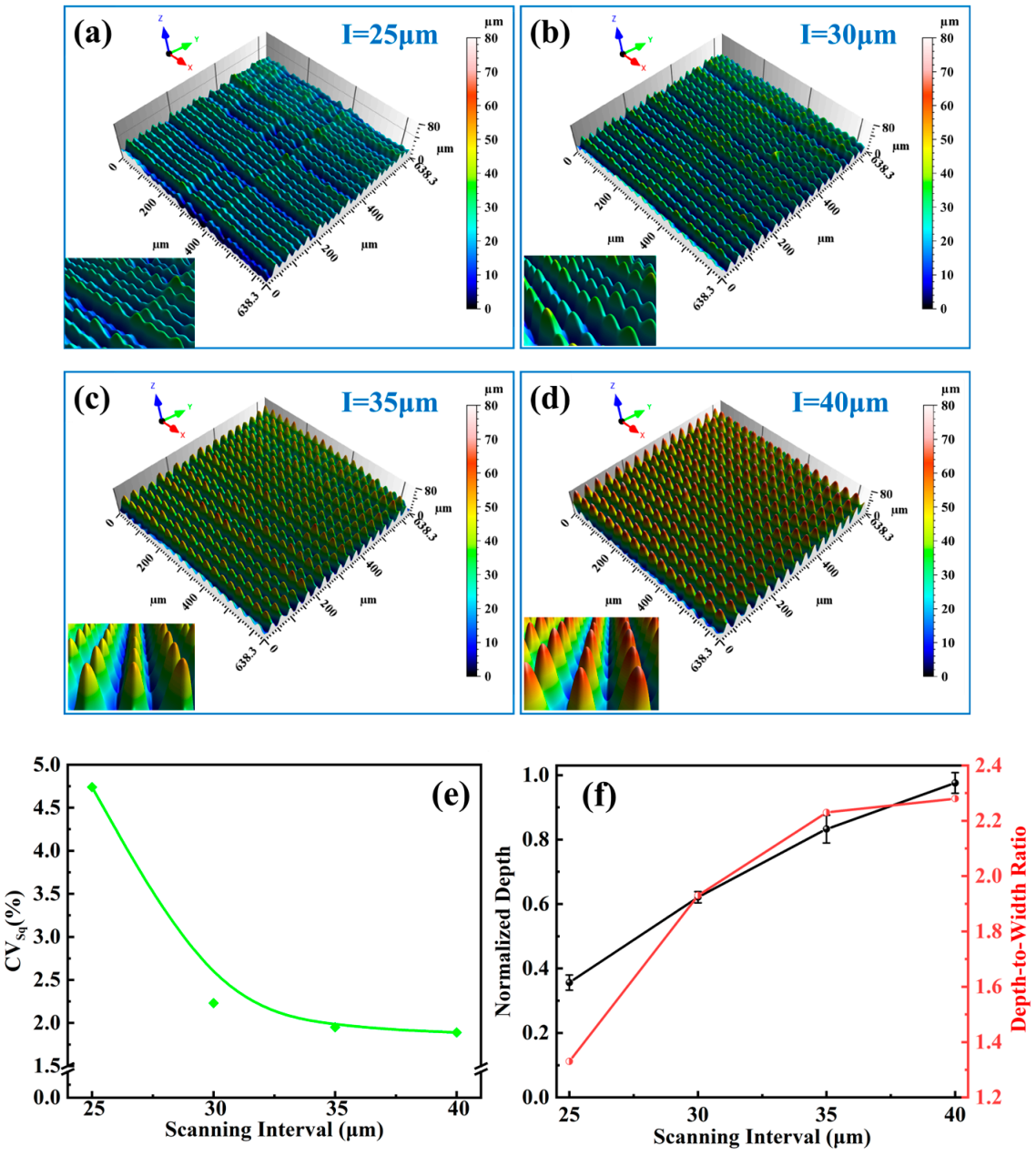


Figure 3. Morphology at different scanning intervals: (**a**) 25 μm, (**b**) 30 μm, (**c**) 35 μm, (**d**) 40 μm. The illustration in the lower left corner is the corresponding high-magnification topography image. (**e**) CV_{Sq} changes under different scanning intervals. (**f**) Dependence of normalized depth on scanning interval, along with the corresponding depth-to-width ratio.

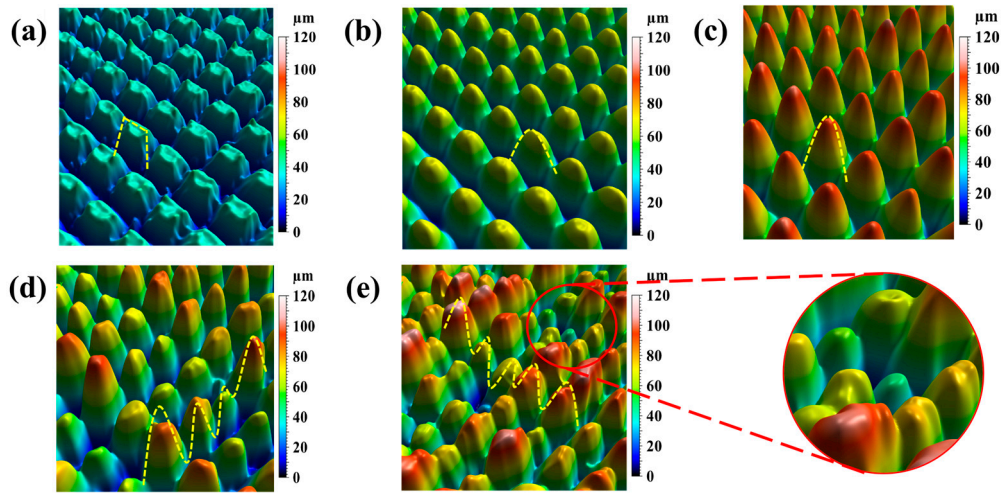


Figure 4. Three-dimensional views of the conical array morphology under different energies, (**a**–**e**) corresponding to energies of 9 μJ, 14 μJ, 19 μJ, 24 μJ, 29 μJ (corresponding to a fluence of 1.273 J/cm^2, 1.981 J/cm^2, 2.688 J/cm^2, 3.395 J/cm^2, and 4.103 J/cm^2), respectively. The profile of the conical structure is depicted with a dotted line (yellow). (**a**–**c**) The profiles of individual units remain nearly identical. Pronounced height variations are observed among the unit profiles in (**d**,**e**).

Scanning electron microscopy was used to further observe the microcone array structure of the orthogonal scanning strategy, as shown in Figure 5. The micron-scale conical unit structures are evenly arranged, and hierarchical micro- and nanostructures are formed on the surface of the conical structure. Figure 5b,c shows a local magnification of the surface of a conical unit structure, on which wavelength-scale LIPSS are induced by the interference between the laser and surface plasmons. The incident laser light is optically scattered by the surface roughness, which may trigger the excitation of surface plasmon polaritons (SPPs). The interference between the excited SPPs and the incident light then modulates the spatial distribution of the deposited laser fluence, giving rise to periodic energy deposition and selective ablation, and eventually resulting in the formation of LIPSS [30,31]. As shown in Figure 5d, the nanoscale particle structure can be observed under further magnification. Affected by Rayleigh-Taylor instability or capillary instability, laser ablation forms micro-nanotextures and nanowrinkles, accompanied by the redeposition of particles and the formation of nanopores, constituting a hierarchical rough structure spanning the nanometer to micrometer scale [6,17]. Figure 5e shows the reflectivity of the orthogonal scanning strategy at different wavelengths. When E = 19 μJ (F = 2.688 J/cm^2), the best antireflection performance is achieved (consistent with the previous analysis), with an average reflectance of 1.61% in the UV-VIS range and 4.38% in the NIR spectrum. The lowest measured reflectance occurs in the UV–VIS region, reaching only 0.94%, which is comparable to or even surpasses representative results reported in existing studies on laser-textured copper surfaces [6,11]. The highest reflectance is observed near 2500 nm, but does not exceed 7%. The antireflection curve of this structure conforms to the general characteristics of micro-nanostructure antireflection surfaces, which are lower in the short-wavelength band and higher in the long-wavelength band [12,16]. Particle agglomeration and nanoscale depressions can induce angular scattering and multiple internal reflections. Moreover, because their characteristic dimensions are comparable to the wavelengths in the UV-VIS region, localized near-field optical effects may be enhanced, thereby improving the antireflection performance in this spectral range [5,6,8,15]. Meanwhile, wavelength-scale LIPSS may introduce Bragg scattering, which couples part of the incident light from the specular direction into lateral scattering channels, increases the optical path length, and assists in a smoother optical transition from the visible to near-infrared region [32].

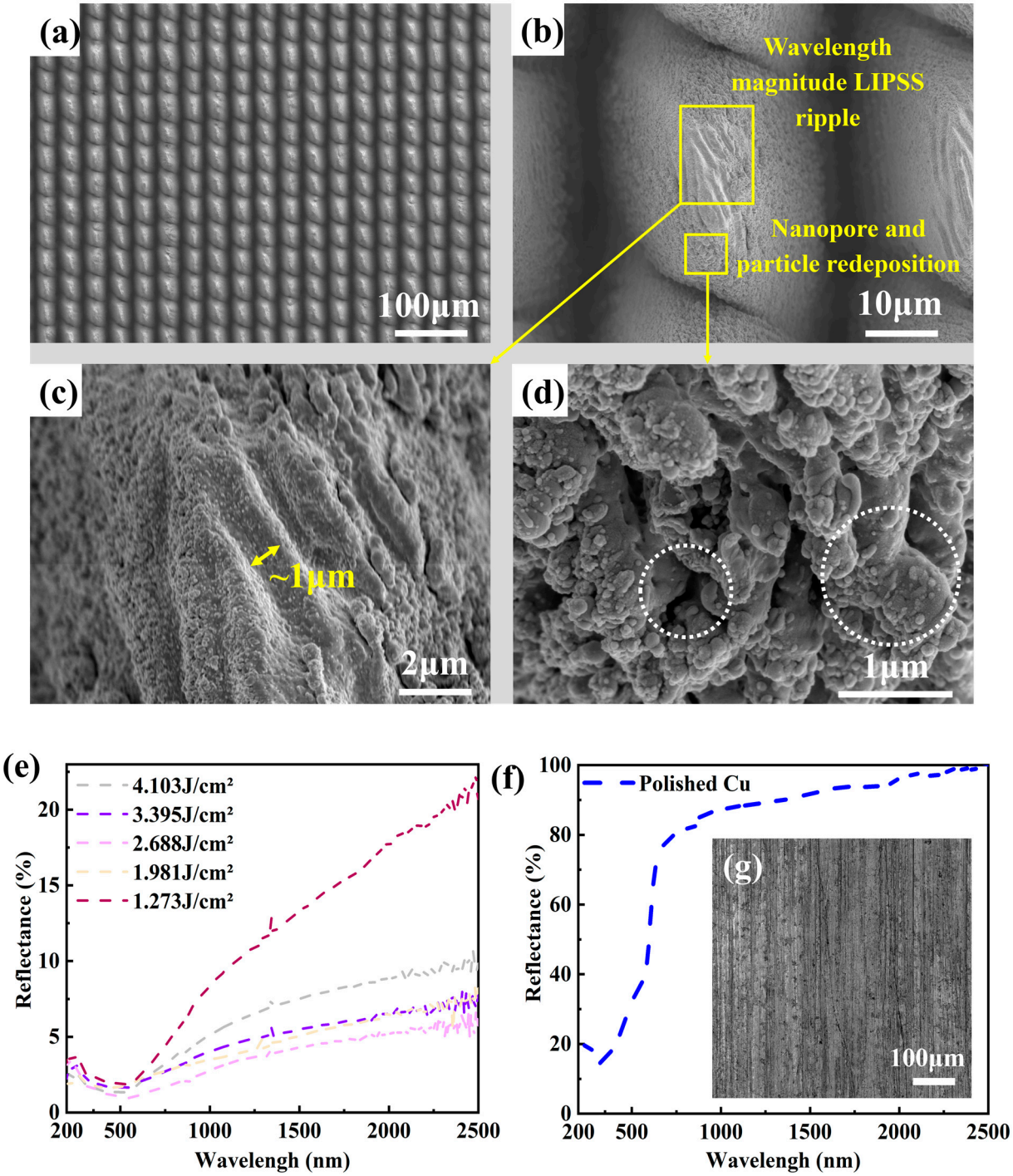


Figure 5. For clarity, all SEM images in this figure are rotated 90° counterclockwise relative to the original sample orientation. (**a**–**d**) SEM images of the conical array morphology (magnification of 200 times, 2000 times, 10,000 times, and 30,000 times). (**e**) Reflection curves under different energies of a 90° scanning strategy. For reference, the reflectance of the polished Cu substrate is displayed in (**f**), while the morphological image of the pristine surface is presented in (**g**). Rectangles (yellow) mark the nanopores, redeposited particles, and wavelength-scale LIPSS ripple, respectively.

3.2. Non-Orthogonal Scanning Strategies

Typical light-trapping structures include hole-like structures [20,30], parabolic structures [33], and conical structures [12,29]. Most structures rely on laser ablation and enhance surface roughness by plasma-mediated redeposition. In contrast, the Marangoni effect-driven melt migration and stacking formation mechanism offers an alternative fab-

rication route [34]. In the non-orthogonal scanning strategy, the crossing angle between adjacent scan tracks differs from that in the orthogonal scanning mode, leading to a distinct anisotropy in local energy deposition. When the adjacent scan tracks are closer to each other, and the directional difference between them becomes smaller, the temperature field and melt-pool flow within the laser-irradiated region are more likely to undergo directional superposition. Driven by the combined effects of vapor recoil pressure, Marangoni-driven melt flow, and capillary pressure, the molten layer may be redistributed preferentially toward the intersecting region and the local depressions, thereby promoting further deepening of the recessed features [16,35]. This behavior can be attributed to the fact that the track-intersection region acts as a zone of enhanced laser energy accumulation, where the local temperature reaches its maximum, and the temperature-dependent surface-tension gradient becomes more pronounced, leading to the redistribution of molten metal around the central depressed region. In parallel, vapor recoil pressure induced by laser pulses further destabilizes the melt layer and facilitates material expulsion. Local remelting and re-evaporation may occur repeatedly, resulting in a synergistic process involving melt redistribution, evaporative removal, and continuous morphology evolution. In addition, the faster accumulation of deposited energy promotes the overlap between the ablation zone and the heat-affected zone, further inducing sidewall remelting and partial structural collapse. Consequently, microcavity-like morphologies are more favorably formed under the non-orthogonal scanning strategy. This study uses two non-orthogonal scanning strategies, 60° cross and 45° cross, to form specific structures by driving the molten pool flow, and fabricate two types of structures, namely flat microcavity and composite microcavity.

3.2.1. 60° Scanning Strategy

As shown in Figure 6, under the 60° cross-scanning strategy, the surface morphology evolves with changes in energy deposition. Under the high repetition rate of 1 MHz, the time interval between adjacent pulses is only 1 μs; thus, the irradiated region cannot fully dissipate the deposited heat before the arrival of subsequent pulses. This heat accumulation raises the local temperature and prolongs the lifetime of the molten layer. As a result, a thicker and more continuous melt pool is generated, in which the viscosity-related resistance to melt redistribution is reduced, and the liquid metal becomes more susceptible to recoil-pressure-driven expulsion and temperature-gradient-induced Marangoni flow. During successive pulse irradiation, this process is repeated through remelting and redeposition, causing molten copper to accumulate and form microcavity structures. When ν = 100 mm/s, the pulse overlap is low, the energy deposition is insufficient, and the surface of the material forms a hexagonal honeycomb-like flat microcavity array with a pitch of 35 μm, which follows the geometric relationship of an equilateral triangle, as shown in Figure 6a. Reducing the scanning speed increases the energy deposited per unit area, the ablation intensity and vapor recoil pressure increase [1,27], the melting and material accumulation become more pronounced, and the morphology changes to a composite microcavity structure, as shown in Figure 6b.

The microstructure was characterized by SEM. As shown in Figure 7a,e, the spatial arrangement characteristics of the two microcavity structures closely follow the laser scanning trajectories. On the picosecond time scale, laser interaction with the material begins with electron excitation, which transfers heat to the crystal lattice via the electron-phonon synergistic effect. Thermal diffusion then determines the spatial scale of the melt zone [18]. In the flat microcavity structure, nanoscale wrinkles and redeposited particles are observed on the walls and bottom of the microcavities, as shown in Figure 7b–d. In the composite microcavity structure, the cavity sidewalls form a semi-enclosed geometry, as shown in Figure 7f–h, introducing multiple medium-air interface boundaries [12,14], which

redistributes the reflected light from a single interface to multiple interfaces, alleviates the abrupt refractive index change, and thereby weakens the overall reflectance. Periodic LIPSS stripes are distributed on the side walls of the cavity, as shown in Figure 7g, which contributes to the suppression of specular reflection [32]. A higher pulse overlap ratio intensifies laser ablation, forming a rich plasma plume that falls back to the surface as redeposited material under the influence of gravity. Subsequently, sintering induced by the tail-end of the Gaussian laser beam profile promotes the formation and adhesion of dense nanoparticles on the surface [8,23], making the wrinkles more pronounced and increasing particle redeposition. This facilitates multiple scattering, guiding incident light efficiently into the microcavity, and reducing surface reflection loss [15].

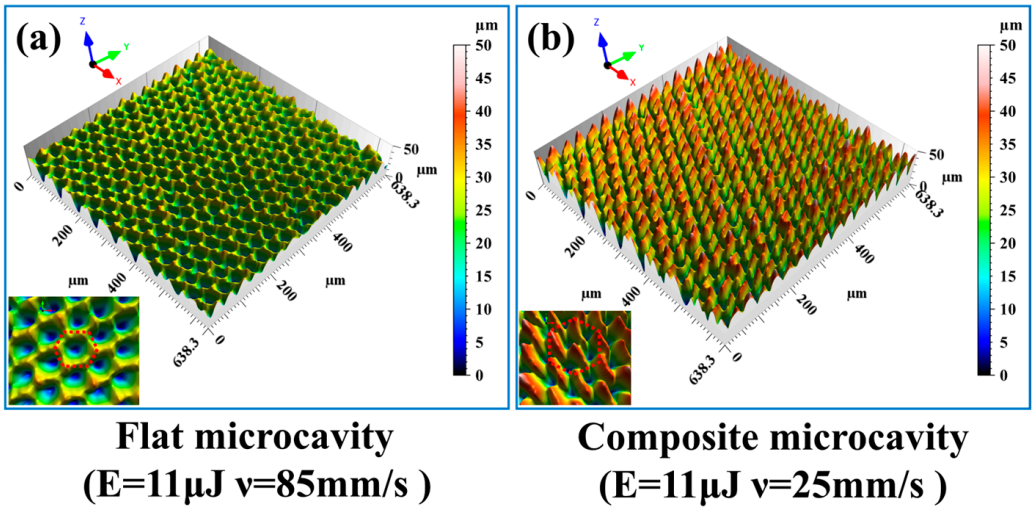


Figure 6. Different forms of microcavity structure: (**a**) flat microcavity, (**b**) composite microcavity. The illustration in the lower left corner is the corresponding high-magnification topography image.

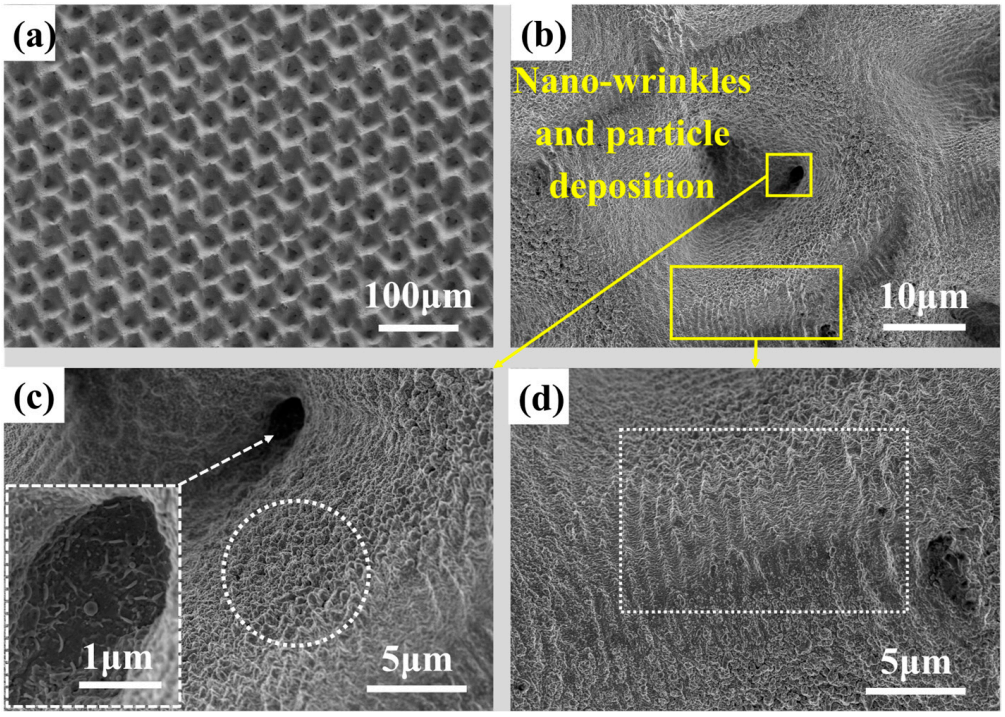


Figure 7. *Cont.*

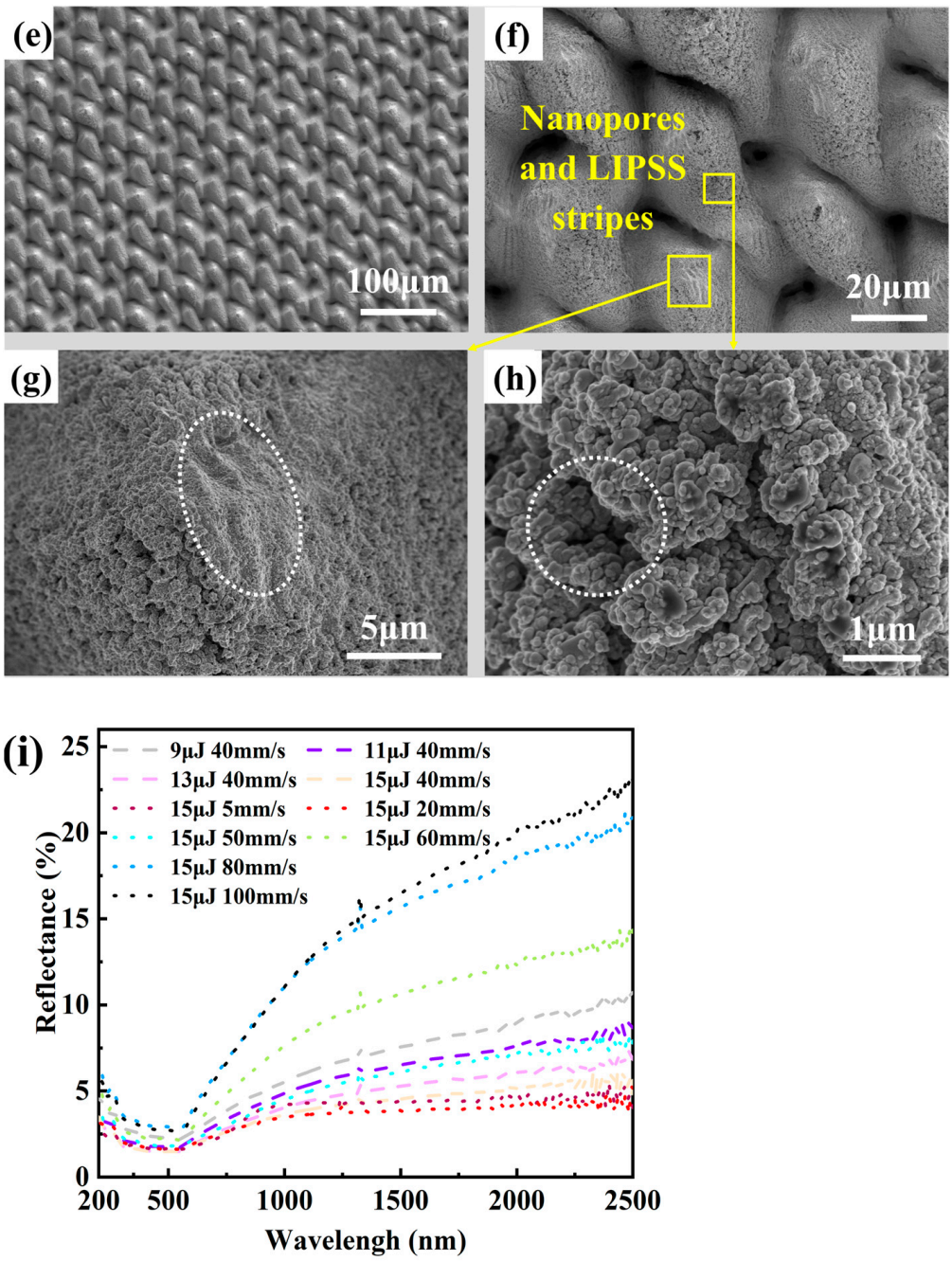


Figure 7. SEM images of the two representative structures fabricated using a 60° scanning strategy. For clarity, all SEM images in this figure are rotated 90° counterclockwise relative to the original sample orientation. (**a**) flat microcavity and (**e**) composite microcavity, magnification of 200 times. (**b**–**d**) and (**f**–**h**) show the corresponding higher-magnification views of the flat microcavity (magnification of 2000 times, 5000 times, and 5000 times) and composite microcavity (magnification of 1000 times, 5000 times, and 20,000 times), respectively. (**i**) Reflection curves under different energies and scanning speeds of a 60° scanning strategy. Rectangles (yellow) represent nanopores, LIPSS stripes, nanowrinkles, and particle deposition, respectively. The hole in the (**c**) is further enlarged (20,000 times).

Figure 7i shows the reflectivity of the 60° scanning strategy. When $\nu \geq 60$ mm/s, flat microcavities are preferentially formed; the relatively large cavity size limits geometrical light-trapping. Part of the incident light is directly reflected, and the reflectivity is relatively high. When $\nu \leq 60$ mm/s, the structure gradually transforms into a composite microcavity, and the number of surface nanoparticles increases significantly (as shown in Figure 7h).

The reflectance decreases significantly, reaching its lowest when ν = 20 mm/s. The average reflectance in the UV-VIS range is 2.13%. Although the reflectance continues to rise between 800 nm and 2500 nm, the spectral response remains stable, with a maximum increment of only ~40%. In addition, it was ~2% lower than that of the 90° orthogonal scanning strategy, with the maximum value not exceeding 5%. This combination of low and spectrally flat reflectance is particularly remarkable for copper surfaces, as the intrinsically large optical constants of copper generally make reflectance in the NIR region difficult to suppress, and previous studies have reported a marked increase in reflectance with wavelength [7,11,29]. The 60° scanning strategy features threefold rotational symmetry, which spatially reduces directional differences in energy deposition and thereby alleviates the energy anisotropy commonly induced by unidirectional scanning. As a result, the surface tends to develop a more geometrically balanced morphology in different directions, as shown in Figure 7e,f. Benefiting from the synergistic effect of microscale cavity depth and semi-enclosed sidewall geometry, incident light can undergo repeated internal reflections within the cavities, where most of the light energy is progressively absorbed, and only a limited fraction can be outcoupled. This assists in mitigating the sensitivity of the long-wavelength optical response to the intrinsically high reflectivity of copper. In addition, the relatively symmetric and periodic topography contributes to reduced angular sensitivity, enabling incident light to be more effectively confined through multiple internal reflections and leading to a more stable absorption enhancement in the long-wavelength region. In addition, when the scanning speed is further reduced to 5 mm/s, the energy deposition is too large at this point, the structure becomes deteriorated, and the reflectivity rises again.

3.2.2. 45° Scanning Strategy

For the 45° cross-scanning strategy, because the density of scanning lines is further increased, the line interval was set to 40 μm to control the heat-affected zone (HAZ). Under the high repetition rate of 1 MHz, the microcavity structures are hardly formed in a single step. Instead, these features are more likely the result of pulse-to-pulse feedback-driven morphological evolution. The microcavities may be progressively developed through repeated cycles of melting, local collapse, resolidification, and subsequent ablation-induced material removal. This process is associated with enhanced local heat accumulation under repeated high-overlap irradiation, which promotes continuous morphology reconstruction. As shown in Figure 8, the morphology is characterized by an array of matrix-like circular microcavities. When ν = 85 mm/s, the energy deposition is low, and the morphology is flat, as shown in Figure 8a. When ν = 25 mm/s, with the increase of pulse overlap ratio, the deposition and ablation linewidths increase, and the originally shallow topographical features gradually develop into pronounced protrusions and depressions [24], forming a composite microcavity structure, as shown in Figure 8b.

SEM images of the flat microcavity structure using the 45° cross-scanning strategy are shown in Figure 9a–d. The overall structure exhibits a planar distribution, and the transition between the microcavity opening surface and the base plane is gentle. The cavity-bottom depression exhibits steep sidewalls and becomes steeper with increasing depth. Nanoscale linear structures formed inside the microcavity exhibit a high aspect ratio and a low effective filling factor, which may mitigate the abrupt air–surface refractive index discontinuity and thereby help suppress reflection [15,17]. The composite microcavity structure is shown in Figure 9e–h. Dense line scanning leads to the formation of abundant nanoparticles deep inside the microcavity depressions, which further enhances the light absorption of the structure. Wavelength-scale LIPSS are clearly observed in both flat and composite microcavities, and the coverage is higher than that in the 60° scanning strategy. At this point, the structural antireflection mechanism is mainly based on synergistic optical

modes. As shown in Figure 9f, self-organized wrinkled features are generated on the microcavity sidewalls under pulsed laser irradiation. These features give rise to localized optical resonances with the incident light, thereby confining light within the microcavities and promoting multiple scattering and internal reflection, which enhances antireflection performance in the NIR band [4,27].

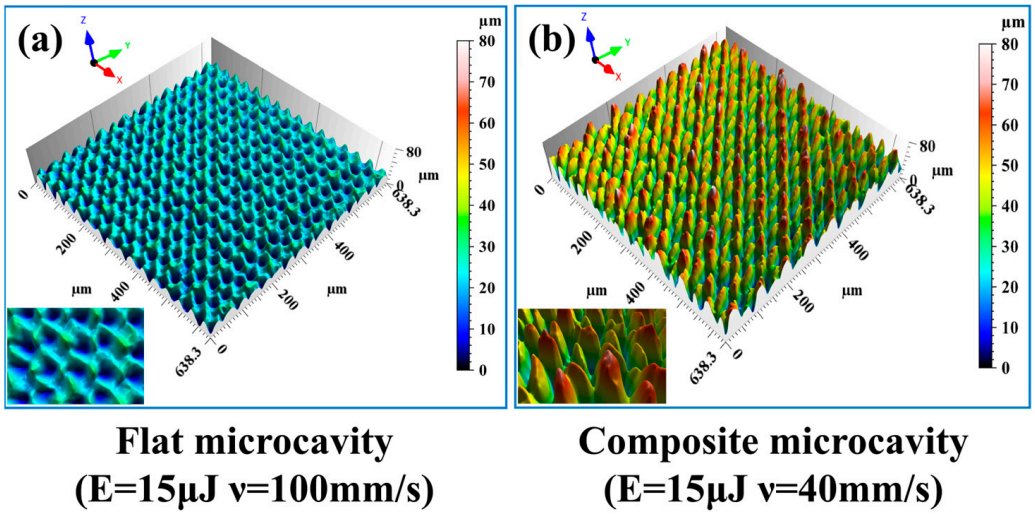


Figure 8. Different forms of microcavity structure: (**a**) flat microcavity, (**b**) composite microcavity. The illustration in the lower left corner is the corresponding high-magnification topography image.

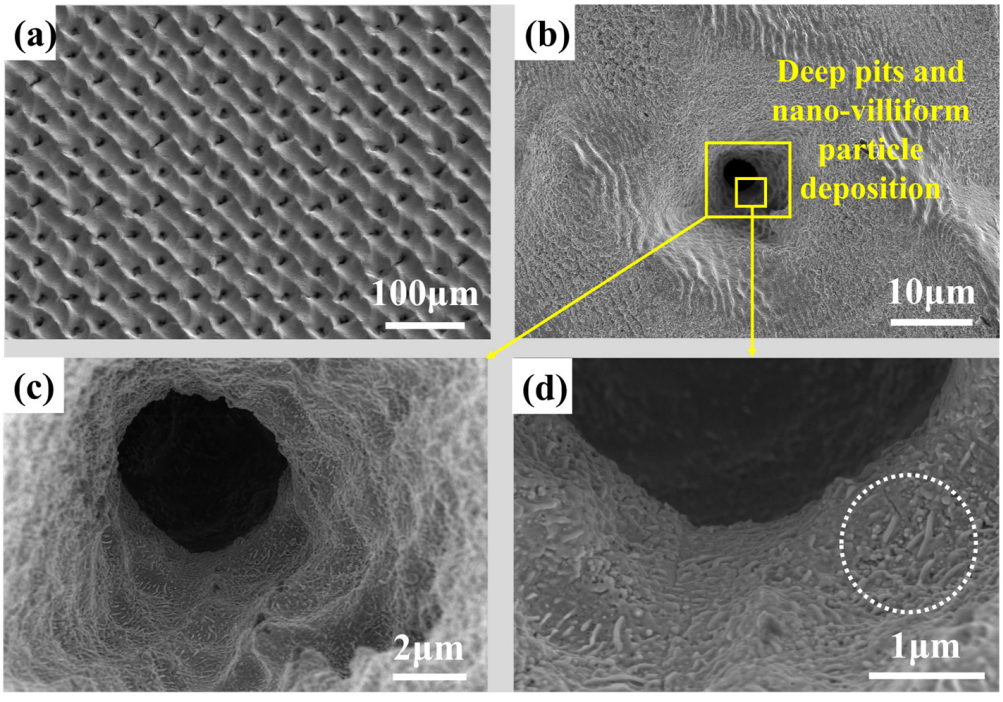


Figure 9. *Cont.*

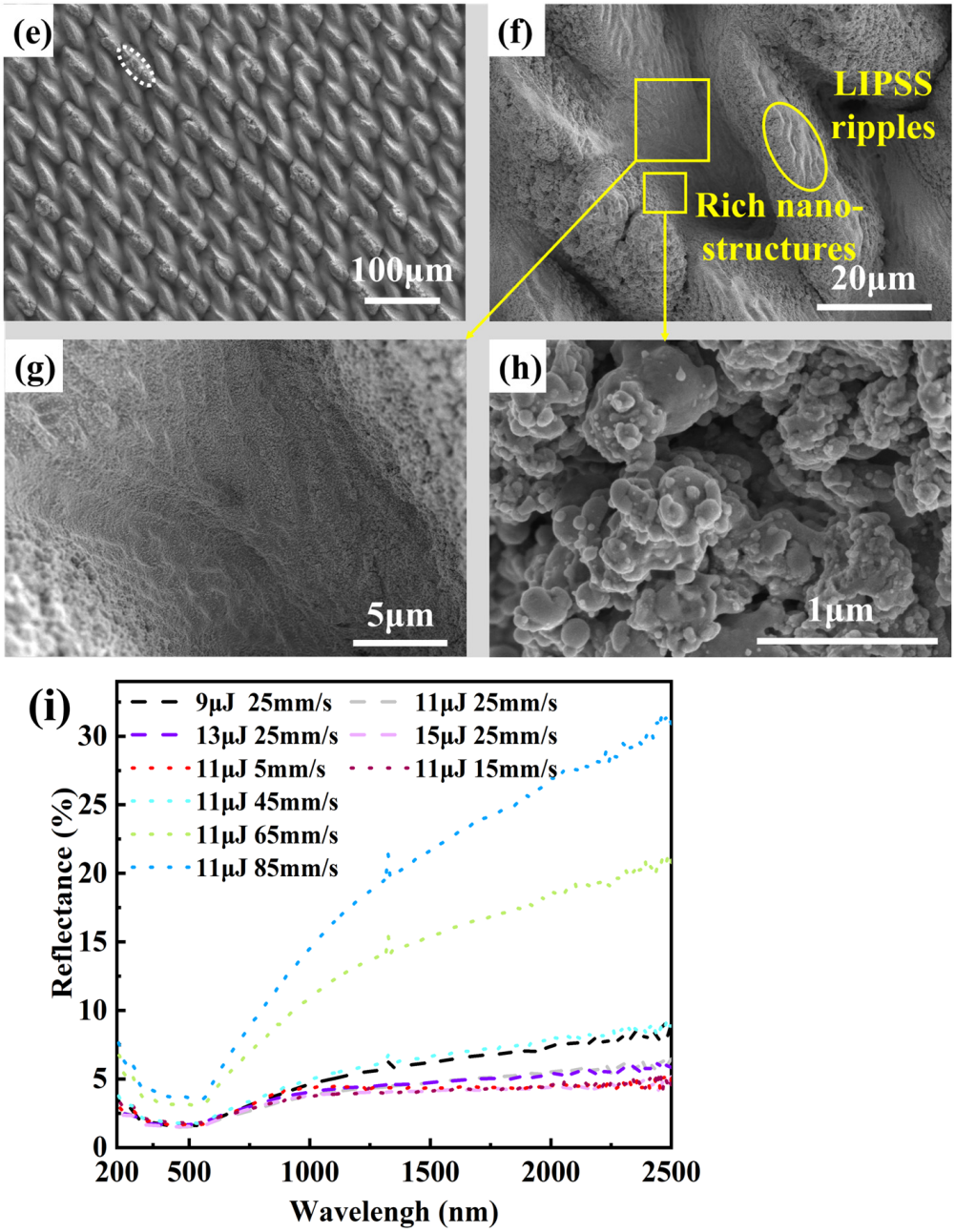


Figure 9. SEM images of the two representative structures fabricated using a 45° scanning strategy. For clarity, all SEM images in this figure are rotated 90° counterclockwise relative to the original sample orientation. (**a**) flat microcavity and (**e**) composite microcavity, magnification of 200 times. (**b**–**d**) and (**f**–**h**) show the corresponding higher-magnification views of the flat microcavity (magnification of 2000 times, 10,000 times, and 30,000 times) and composite microcavity (magnification of 1500 times, 5000 times, and 50,000 times), respectively. (**i**) Reflection curves under different energies and scanning speeds of a 45° scanning strategy. The rectangle (yellow) represents rich nanostructures, deep pits, and villiform nanoparticle redeposition, respectively.

Figure 9i shows the reflectivity of the 45° scanning strategy. At a constant pulse energy, as the scanning speed gradually decreases from the high-speed state of ν = 85 mm/s, the overall reflectance decreases rapidly, reaching the minimum at ν = 15 mm/s. This process corresponds to the evolution of the microcavity morphology. At ν = 15 mm/s, the average reflectance in the UV to VIS light spectrum range is 2.31%. It only increases slightly after 800 nm. The increase is mainly between 2000–2500 nm, and the average reflectance is ~4.68%. Further comparison of the antireflection curves of ν = 15 mm/s and

ν = 5 mm/s shows that the two surfaces exhibit nearly identical antireflection performance. This arises from the intrinsically high overlap density of this strategy, which makes the energy deposition more likely to reach saturation than the other two strategies. At this point, further reducing the scanning speed contributes little to morphology evolution or antireflection improvement.

3.3. Characterization

In order to further compare the light absorption performance of the three strategies in the UV-VIS and NIR spectral ranges, the best-performing reflectance curve of the three scanning strategies is compared, as shown in Figure 10a. Different scanning strategies correspond to different forms of surface microstructures, and the crossover point between the reflectance spectra of the two morphologies is located near 1300 nm. In the short wavelength spectral range starting from 200 nm, the microcone array structure shows superior antireflection performance. Beyond the crossover point and up to 2500 nm, the reflectance of the microcavity structure is significantly lower than that of the microcone array structure.

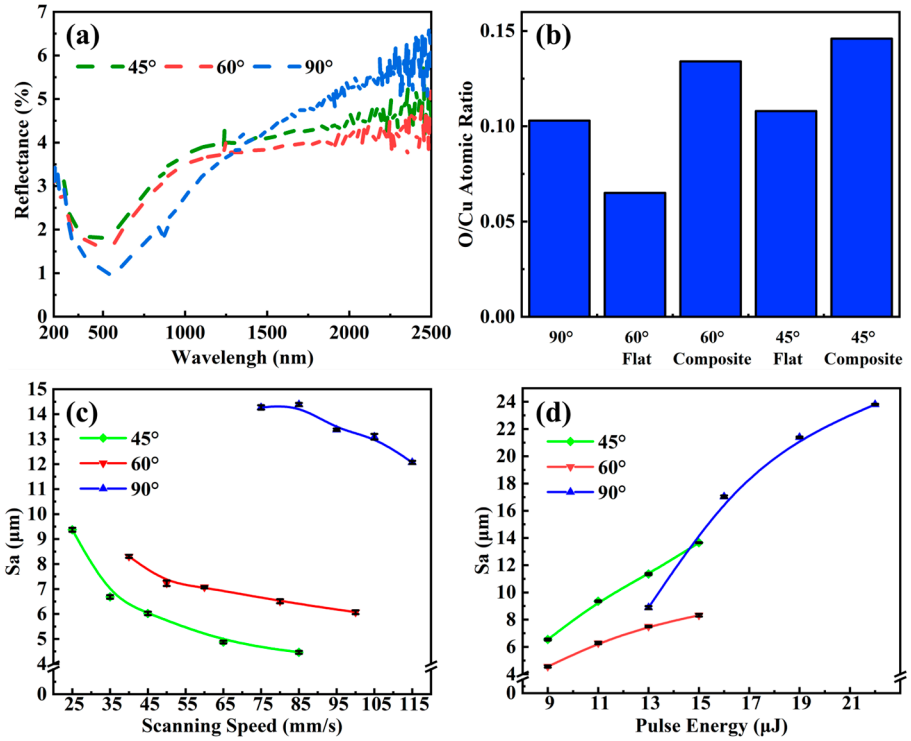


Figure 10. (**a**) Best-performing antireflection spectra for each strategy. (**b**) O/Cu atomic ratio characterized by EDS. (**c**,**d**) Surface roughness of each scanning strategy as a function of laser energy and scanning speed.

The elemental composition and surface roughness of the five morphologies prepared by the three strategies were further characterized, as shown in Figure 10b–d. In order to characterize the relative degree of oxidation, the O and Cu contents in each morphology were detected and analyzed by an energy dispersive X-ray spectrometer (EDS), and the atomic ratio (O/Cu) of the two elements was calculated, as shown in Figure 10b. According to the EDS results, when comparing the 45°, 60°, and 90° strategies, the oxygen content shows a decreasing trend as the scan-line density decreases. The 45° composite microcavity structure has the highest oxygen content, and the 60° composite microcavity structure has the second highest degree of oxidation, but is higher than the 90° scanning strategy. Figure 10c,d compares the effects of pulse energy and scanning speed on surface roughness

under different scanning strategies. The roughness trends under the 60° and 45° strategies are similar. Due to the smaller scan line density of the 90° orthogonal scanning strategy, the difference in melting behavior between the ablation center and peripheral regions becomes more pronounced, and the structure height fluctuates significantly, resulting in higher roughness than in the non-orthogonal scanning strategies.

In the 200–1300 nm band, the incident wavelength is comparable to the characteristic dimensions of surface features such as nanoparticles and LIPSS, making localized near-field optical effects more pronounced, thereby enhancing the antireflection effect [5,8,12,17]. Moreover, the larger surface roughness indicates a stronger micron-scale topographic undulation, which is generally associated with a more pronounced geometrical light-trapping effect and thus favors reflectance suppression in the short-wavelength region [15]. As the 90° orthogonal scanning strategy shows the largest roughness, it exhibits superior antireflection performance in this spectral range. In the longer-wavelength range of 1300–2500 nm, the contribution of geometrical light-trapping becomes less dominant. Instead, previous studies have suggested that the influence of the wavelength-dependent dielectric response of the modified surface on reflectance gradually increases in this spectral range [36]. In addition, other studies have indicated that oxidation of Cu may alter the near-surface optical response by modifying the dielectric response of the material, thereby contributing to enhanced absorption in the longer-wavelength region [17,37]. Therefore, the non-orthogonal scanning strategies are more favorable. However, it should be noted that the evolution trend of oxide content is inconsistent with the reflectance trend, and its contribution to reducing reflection is limited [7]. A dense oxide layer formed by excessive oxidation can deteriorate antireflective performance [17]. The microcone array morphology prepared by orthogonal scanning achieves a minimum reflectivity of 0.94% in the range of 200–1300 nm. The microcavity morphology prepared by non-orthogonal scanning overcomes the challenge of achieving effective antireflection in the long-wavelength range of 1300–2500 nm, with the reflectance maintained below 5%. The average reflectance of the 60° strategy is only 4.06%, and the fabrication route is simple and flexible. Because different scanning strategies yield distinct antireflection characteristics, patterned blackened surfaces that preferentially enhance short-wavelength or long-wavelength absorption can be selectively fabricated in different areas of the same surface.

4. Conclusions

This study goes beyond conventional laser blackening of copper by showing that the scanning strategy is not merely a processing detail, but a key parameter for governing morphology selection and spectral antireflection behavior. The orthogonal scanning strategy (90°) was employed to construct a microcone array structure, and the non-orthogonal scanning strategies (60° and 45°) were adopted to fabricate a variety of antireflection structures, including flat microcavity and composite microcavity. Owing to the synergistic effects of LIPSS and localized near-field optical effects, all these structures achieve broadband antireflection. Optical measurement results show that the microcone array structure has excellent antireflection performance in the UV-VIS spectrum range, with a minimum reflectance of 0.94%. The composite microcavity structure exhibits superior performance in the NIR band. The maximum reflectance occurs near 2500 nm and remains around 4%, and the reflectance remains relatively stable over 800–2500 nm. This work establishes a controllable link between scanning trajectory, multiscale structural morphology, and band-dependent optical response, providing a practical fabrication route for designing functionalized metallic surfaces for specific light absorption bands. Future work will focus on the effect of pulse burst mode irradiation on morphology, explore the role of laser polarization (e.g., circular polarization) in morphology formation, and evaluate the antireflection performance

of the structure under different incident angles to assess its potential for applications in extreme environments.

Author Contributions: Conceptualization, J.Z. and Z.H.; methodology, J.Z. and Z.C.; validation, J.Z.; formal analysis, J.Z. and Y.C.; investigation, J.Z.; resources, Z.H., Z.C. and Y.C.; data curation, J.Z. and Y.C.; writing—original draft preparation, J.Z.; writing—review and editing, J.Z., Z.C. and Z.H.; visualization, J.Z.; supervision, Z.C. and Z.H.; project administration, Z.H. All authors have read and agreed to the published version of the manuscript.

Funding: This research received no external funding.

Data Availability Statement: The original contributions presented in this study are included in the article. Further inquiries can be directed to the corresponding author.

Conflicts of Interest: The authors declare no conflicts of interest.

Abbreviations

The following abbreviations are used in this manuscript:

LIPSS	Laser-induced periodic surface structure
SPPs	Surface plasmon polaritons
ROI	Region of interest
HAZ	Heat affected zone
EDS	Energy dispersive X-ray spectrometer

References

1. Ahmmed, K.M.T.; Grambow, C.; Kietzig, A.-M. Fabrication of Micro/Nano Structures on Metals by Femtosecond Laser Micromachining. *Micromachines* **2014**, *5*, 1219–1253. [CrossRef]
2. Wang, H.; Deng, D.; Zhai, Z.; Yao, Y. Laser-processed functional surface structures for multi-functional applications—A review. *J. Manuf. Process.* **2024**, *116*, 247–283. [CrossRef]
3. Adibekyan, A.; Kononogova, E.; Monte, C.; Hollandt, J. High-Accuracy Emissivity Data on the Coatings Nextel 811-21, Herberts 1534, Aeroglaze Z306 and Acktar Fractal Black. *Int. J. Thermophys.* **2017**, *38*, 89. [CrossRef]
4. Fan, P.; Wu, H.; Zhong, M.; Zhang, H.; Bai, B.; Jin, G. Large-scale cauliflower-shaped hierarchical copper nanostructures for efficient photothermal conversion. *Nanoscale* **2016**, *8*, 14617–14624. [CrossRef] [PubMed]
5. Fan, P.; Bai, B.; Zhong, M.; Zhang, H.; Long, J.; Han, J.; Wang, W.; Jin, G. General Strategy toward Dual-Scale-Controlled Metallic Micro–Nano Hybrid Structures with Ultralow Reflectance. *ACS Nano* **2017**, *11*, 7401–7408. [CrossRef]
6. Fan, P.; Bai, B.; Jin, G.; Zhang, H.; Zhong, M. Patternable fabrication of hyper-hierarchical metal surface structures for ultrabroadband antireflection and self-cleaning. *Appl. Surf. Sci.* **2018**, *457*, 991–999. [CrossRef]
7. Fan, P.; Zhong, M.; Li, L.; Huang, T.; Zhang, H. Rapid fabrication of surface micro/nano structures with enhanced broadband absorption on Cu by picosecond laser. *Opt. Express* **2013**, *21*, 11628–11637. [CrossRef]
8. Fan, P.; Zhong, M.; Bai, B.; Jin, G.; Zhang, H. Tuning the optical reflection property of metal surfaces via micro–nano particle structures fabricated by ultrafast laser. *Appl. Surf. Sci.* **2015**, *359*, 7–13. [CrossRef]
9. Calvani, P.; Bellucci, A.; Girolami, M.; Orlando, S.; Valentini, V.; Polini, R.; Trucchi, D.M. Black diamond for solar energy conversion. *Carbon* **2016**, *105*, 401–407. [CrossRef]
10. Caragnano, S.; De Palo, R.; Sfregola, F.A.; Gaudiuso, C.; Mezzapesa, F.P.; Patimisco, P.; Ancona, A.; Volpe, A. Femtosecond Laser-Engineered Molds for Long-Term Stable Superhydrophobic Polydimethylsiloxane (PDMS) Surfaces. *Adv. Mater. Interfaces* **2025**, *12*, e00808. [CrossRef]
11. He, Z.; Xie, X.; Long, J. Antireflective copper surfaces fabricated by low-cost nanosecond lasers for efficient photothermal conversion and desalination. *J. Laser Appl.* **2019**, *31*, 022506. [CrossRef]
12. Qi, J.Y.; Liu, X.Q.; Liu, Z.J.; Zhang, X.; Li, C.; Chen, Q.D.; Wang, L.; Sun, H.B. Ultrawide Spectrum Metallic Plane Blackbody with Extremely High Absorption from 0.2 to 25 μm. *Adv. Sci.* **2024**, *12*, 2411448. [CrossRef] [PubMed]
13. Leem, J.W.; Song, Y.M.; Lee, Y.T.; Yu, J.S. Effect of etching parameters on antireflection properties of Si subwavelength grating structures for solar cell applications. *Appl. Phys. B* **2010**, *100*, 891–896. [CrossRef]
14. Xue, L.; Yang, J.; Yang, Y.; Wang, Y.; Zhu, X. Creation of periodic subwavelength ripples on tungsten surface by ultra-short laser pulses. *Appl. Phys. A* **2012**, *109*, 357–365. [CrossRef]

15. Chen, T.; Wang, W.; Tao, T.; Pan, A.; Mei, X. Broad-Band Ultra-Low-Reflectivity Multiscale Micro–Nano Structures by the Combination of Femtosecond Laser Ablation and In Situ Deposition. *ACS Appl. Mater. Interfaces* **2020**, *12*, 49265–49274. [CrossRef]
16. Long, J.; Cao, Z.; Lin, C.; Zhou, C.; He, Z.; Xie, X. Formation mechanism of hierarchical Micro- and nanostructures on copper induced by low-cost nanosecond lasers. *Appl. Surf. Sci.* **2019**, *464*, 412–421. [CrossRef]
17. Liu, H.; Hu, J.; Jiang, L.; Zhan, S.; Ma, Y.; Xu, Z.; Lu, Y. Ultrabroad antireflection urchin-like array through synergy of inverse fabrications by femtosecond laser-tuned chemical process. *Appl. Surf. Sci.* **2020**, *528*, 146804. [CrossRef]
18. Zhang, D.; Ranjan, B.; Tanaka, T.; Sugioka, K. Carbonized Hybrid Micro/Nanostructured Metasurfaces Produced by Femtosecond Laser Ablation in Organic Solvents for Biomimetic Antireflective Surfaces. *ACS Appl. Nano Mater.* **2020**, *3*, 1855–1871. [CrossRef]
19. Kaakkunen, J.J.J.; Paivasaari, K.; Kuittinen, M.; Jaaskelainen, T. Morphology studies of the metal surfaces with enhanced absorption fabricated using interferometric femtosecond ablation. *Appl. Phys. A* **2008**, *94*, 215–220. [CrossRef]
20. Taher, M.A.; Ponnan, S.; Prasad, H.; Rao, D.N.; Naraharisetty, S.R.G. Broadband absorption of nanostructured stainless steel surface fabricated by nanosecond laser irradiation. *Nanotechnology* **2020**, *31*, 175301. [CrossRef]
21. De Palo, R.; Volpe, A.; Patimisco, P.; Zifarelli, A.; Sampaolo, A.; Ancona, A.; Wu, H.; Spagnolo, V. Femtosecond laser fabrication of black quartz for infrared photodetection applications. *Light Adv. Manuf.* **2025**, *6*, 26. [CrossRef]
22. Zhou, H.; Zhang, J.; Bai, B.; Mei, X.; Hao, X.; Song, J.; Guo, G.; Chen, J.; Tian, T.; Zhou, Q.; et al. Ultra-Broadband Plane Blackbody by Ultrafast Laser Induced Surface Hierarchical Structuring and Nanodefect Engineering. *Adv. Mater.* **2026**, *38*, e12727. [CrossRef]
23. Anderson, M.; Kaufman, G.; Ediger, A.; Alexander, D.; Zuhlke, C.; Shield, J.E. Formation mechanism of micro/nanoscale structures on picosecond laser pulse processed copper. *Mater. Today Adv.* **2023**, *19*, 100412. [CrossRef]
24. Csizmadia, T. Comparison of the Production of Nanostructures on Bulk Metal Samples by Picosecond Laser Ablation at Two Wavelengths for the Fabrication of Low-reflective Surfaces. *J. Laser Micro/Nanoeng.* **2015**, *10*, 110–118. [CrossRef]
25. Nayak, B.K.; Iyengar, V.V.; Gupta, M.C. Efficient light trapping in silicon solar cells by ultrafast-laser-induced self-assembled micro/nano structures. *Prog. Photovolt. Res. Appl.* **2011**, *19*, 631–639. [CrossRef]
26. Qiao, H.; Yang, J.; Li, J.; Liu, Q.; Liu, J.; Guo, C. Formation of Subwavelength Periodic Triangular Arrays on Tungsten through Double-Pulsed Femtosecond Laser Irradiation. *Materials* **2018**, *11*, 2380. [CrossRef] [PubMed]
27. Ng, C.-K.; Chen, T.; Ju, B.-F.; Chen, Y.-L.; Ma, Y. Pixel-level metal blackbody microcavities via hierarchical laser writing. *Sci. Adv.* **2025**, *11*, eadu0608. [CrossRef] [PubMed]
28. Huang, H.; Yang, L.-M.; Bai, S.; Liu, J. Blackening of metals using femtosecond fiber laser. *Appl. Opt.* **2015**, *54*, 324–333. [CrossRef]
29. Tang, G.; Hourd, A.C.; Abdolvand, A. Nanosecond pulsed laser blackening of copper. *Appl. Phys. Lett.* **2012**, *101*, 231902. [CrossRef]
30. Ahmmed, K.M.T.; Ling, E.J.Y.; Servio, P.; Kietzig, A.-M. Introducing a new optimization tool for femtosecond laser-induced surface texturing on titanium, stainless steel, aluminum and copper. *Opt. Lasers Eng.* **2015**, *66*, 258–268. [CrossRef]
31. Maragkaki, S.; Derrien, T.J.Y.; Levy, Y.; Bulgakova, N.M.; Ostendorf, A.; Gurevich, E.L. Wavelength dependence of picosecond laser-induced periodic surface structures on copper. *Appl. Surf. Sci.* **2017**, *417*, 88–92. [CrossRef]
32. Vorobyev, A.Y.; Makin, V.S.; Guo, C. Brighter Light Sources from Black Metal: Significant Increase in Emission Efficiency of Incandescent Light Sources. *Phys. Rev. Lett.* **2009**, *102*, 234301. [CrossRef]
33. Qin, G.; Dong, Y.; Zhang, P.; Liu, J.; Li, C.; Huang, W.; Hong, Z.; Shen, C.; Jing, X. Broadband absorber coupled with anti-reflection inverted pyramid type all-dielectric microstructure. *Opt. Lasers Eng.* **2023**, *160*, 107288. [CrossRef]
34. Ahmadivand, A.; Pala, N. Absorption Enhancement in Ultrathin Structures Based on Crystalline-Si/Ag Parabola Nanocones Periodic Arrays with Broadband Antireflection Property. *Silicon* **2015**, *9*, 25–29. [CrossRef]
35. Bonse, J.; Gräf, S. Maxwell Meets Marangoni—A Review of Theories on Laser-Induced Periodic Surface Structures. *Laser Photonics Rev.* **2020**, *14*, 2000215. [CrossRef]
36. Car, J.; Pietrzak, K.; Krstulović, N. Determination of dielectric functions of colloidal silver nanoparticles. *Appl. Phys. A* **2025**, *131*, 1028. [CrossRef]
37. Welegergs, G.G.; Gebretinsae, H.G.; Tsegay, M.G.; Bhardwaj, A.; Mathur, S.; Kebede, T.G.; Nuru, Z.Y.; Dube, S.; Maaza, M. Spectrally selective single layered Ag@CuO nanocermet coatings for photothermal application: Green synthesis method. *Opt. Mater.* **2023**, *135*, 113247. [CrossRef]

Disclaimer/Publisher's Note: The statements, opinions and data contained in all publications are solely those of the individual author(s) and contributor(s) and not of MDPI and/or the editor(s). MDPI and/or the editor(s) disclaim responsibility for any injury to people or property resulting from any ideas, methods, instructions or products referred to in the content.